Rare Met. (2022) 41(2):650–662
https://doi.org/10.1007/s12598-021-01831-z

RARE METALS

ORIGINAL ARTICLE

Fabrication of GO-TiO_2/(Ca,Y)F_2:Tm,Yb composites with high-efficiency optical driving photocatalytic activity for degradation of organic dyes and bacteriostasis

Hua Guo, Jun Li, Xian-Rui Zou, Hong-Shui Wang, An Kang,
Huan Zhou, Ming-Jun Li, Xiao-Yan Zhao*

Received: 21 April 2021 / Revised: 7 June 2021 / Accepted: 9 June 2021 / Published online: 13 September 2021

Abstract Development of photocatalytic materials able to profit from the whole spectrum of sun for efficient organic pollution removal and bacterial elimination is a fascinating strategy in environmental engineering. In current work, GO-TiO_2/(Ca,Y)F_2:Tm,Yb, a full-spectrum composite photocatalyst, was prepared via hydrothermal processing with TiO_2/(Ca,Y)F_2:Tm,Yb particles deposited on the surface of graphene oxide (GO). The surface properties of GO-TiO_2/(Ca,Y)F_2:Tm,Yb were characterized using various characterization techniques including X-ray diffraction (XRD), scanning electron microscopy (SEM), X-ray photoelectron spectroscopy (XPS) and Brunauer–Emmett–Teller (BET) surface area analyzer. Besides, ultraviolet–visible (UV–Vis) diffuse reflectance spectroscopy, electron spin resonance (ESR) and other methods were used to systematically explore the photocatalytic mechanism of GO enhancement of TiO_2/(Ca,Y)F_2:Tm,Yb. In photocatalytic degradation study, the degradation rate of methyl orange (MO) was improved by 40% when GO was added into the TiO_2/(Ca,Y)F_2:Tm,Yb system. In addition, the presence of GO also improves the antibacterial ability of TiO_2/(Ca,Y)F_2:Tm,Yb against *Escherichia coli* and *Staphylococcus aureus*. All results reveal high efficacy of GO-TiO_2/(Ca,Y)F_2:Tm,Yb under full spectrum light irradiation, in which (Ca,Y)F_2:Tm,Yb and TiO_2 can improve its utilization of full spectrum sunlight, and GO can enhance adsorption ability of dye and electron–hole pair differentiation ability of TiO_2/(Ca,Y)F_2:Tm,Yb.

Keywords Photocatalysis; Graphene oxide; Up-conversion; Adsorption

1 Introduction

In recent years, photocatalytic technology exhibits potentials in pollution and contamination control. Among photocatalytic materials, TiO_2 has received considerable attention in last two decades due to its photocatalytic activity and sustainable, nonhazardous and economically viable significances. However, photocatalytic use of TiO_2 only works under short wavelength ultraviolet (UV) light, displaying easy photogenerated electron–hole pairs recombination and limited light quantum efficiency [1, 2]. Strategies such as TiO_2 surface modification to reduce recombination rate of photogenerated electron–hole pair and increase light absorption range have been attempted to improve its photocatalytic activity [3–9]. For example, by dispersing holmium nanoparticles onto TiO_2, the degradation rates of rhodamine B and MO under UV irradiation increased from 86.6% and 71.2% to 92.1% and 78.4%, respectively [10]. Besides, SnO_2/TiO_2 nanocomposite showed a 90% removal rate of methylene blue (MB) dye

Hua Guo and Jun Li contributed equally to this work.

H. Guo, A. Kang, X.-Y. Zhao*
School of Civil and Transportation Engineering, Hebei University of Technology, Tianjin 300401, China
e-mail: zhaoxiaoyanhebut@126.com

J. Li
Tianjin Juncheng Dentistry Clinic Co. LTD, Tianjin 300090, China

X.-R. Zou, H.-S. Wang, H. Zhou
School of Materials Science and Engineering, Hebei University of Technology, Tianjin 300000, China

M.-J. Li
Institute of Biophysics, Hebei University of Technology, Tianjin 300401, China

under sunlight irradiation, which is higher than that of SnO_2 (44%) and TiO_2 (40%) alone [11]. In addition, some potential photocatalysts, such as Fe^{3+}/C/S/TiO_2, HfO_2/TiO_2, ZnO/TiO_2 and single-crystal TiO_2/$SrTiO_3$, have also been reported [12–17]. In the field of antimicrobial research, materials such as biodegradable Zn alloys, polydopamine-modified metal–organic frameworks, graphitic carbon nitride-based materials, chitosan/Ag/MoS_2, photo-responsive coating composed of MnO_2 and Cu-doped metal–organic frameworks have been reported for inhibiting bacterium [18–23]. Such attempts with TiO_2 have also been applied. For example, black urchin-like defective TiO_2 was decorated with Ag_3PO_4 nanoparticles, which could exhibit antibacterial efficiency up to 99.8% ± 0.2% and 99.9% ± 0.1% against *E. coli* and *S. aureus* after 20-min light irradiation followed by darkness for 12 h [24]. A rapid photo-sonotherapy was proposed by creating an oxygen deficiency on a titanium (Ti) implant through sulfur (S)-doping (Ti-S-TiO_{2-x}), which reached a high antibacterial efficiency of 99.995% against *Staphylococcus aureus* under 15 min near-infrared (NIR) light and ultrasound treatments [25]. However, the catalytic performance of TiO_2 in the above materials was improved in the absence of full spectrum of light utilization [26]. In our previous work, an up-conversion luminescent material TiO_2/(Ca,Y)F_2:Tm,Yb was developed, capable of converting infrared light to visible light and UV light for full spectrum utilization of sunlight. However, this material is still limited to its light adsorption capacity, agglomeration and other issues. Thus, using porous matrix to support TiO_2, as a strategy to improve its surface area and light adsorption performance as well as avoiding particle agglomeration, is of great interest to solve limitations of as reported TiO_2/(Ca,Y)F_2:Tm,Yb [27, 28].

Graphene oxide (GO) has unique properties (high surface area, significant material absorption performance, excellent optical and electrical properties), and its combination with TiO_2 has aroused great research interest in past decades. For example, Liu et al. [29] deposited self-assembled TiO_2 to large GO sheets at water/toluene interface, showing possibility of charging transfer and inhibiting photogenerated electron–hole recombination of TiO_2 by GO. To the best of our knowledge, there are few reports on the combination of GO and TiO_2 with up-conversion luminescent materials. It is hypothesized that taking the advantage of GO and up-conversion luminescent TiO_2, a full spectrum and highly efficient photocatalyst can be developed. As an attempt to verify this concept, a GO-TiO_2/(Ca,Y)F_2:Tm,Yb composite photocatalyst was prepared via a multistep hydrothermal method. It is hypothesized that the large specific surface area and strong adsorption capacity of GO can be used to realize uniform dispersion of TiO_2/(Ca,Y)F_2:Tm,Yb on GO sheets, and the synergistic effect of them can improve the absorption spectral range and catalytic efficiency of TiO_2 photocatalysts, and enhance the organic degradation ability and antibacterial performance of composite photocatalysts.

2 Experimental

2.1 Materials

All chemicals and reagents were analytically pure. Yttrium chloride (YCl_3, 99.999%), ytterbium chloride ($YbCl_3$, 99.999%) and thulium chloride ($TmCl_3$, 99.999%) were purchased from Grirem Advanced Materials Co., Ltd., Beijing, China. Polyvinylpyrrolidone (PVP) and titanium isopropoxide (TTIP) were purchased from Chemical Reagent No. 3, Tianjin, China. Anhydrous calcium chloride ($CaCl_2$) was purchased from Fuchen Chemical Reagent Co., Ltd., Tianjin, China. Acetylacetone (Hacac), acetic acid (CH_3COOH), polyvinyl alcohol (PVA), ammonium fluoride (NH_4F) and GO were provided by Aladdin Reagent Co., Ltd., Shanghai, China.

2.2 Synthesis of TiO_2/(Ca,Y)F_2:Tm,Yb

In a 50 ml beaker, 0.1388 g $CaCl_2$, 0.025 g PVP, 0.25 ml $TmCl_3$ solution (1×10^{-5} mol·ml^{-1}), 1.25 ml $YbCl_3$ solution of 1×10^{-4} mol·ml^{-1}, 2.487 ml YCl_3 solution (2×10^{-4} mol·ml^{-1}) and 20 ml deionized water were mixed with 15 min magnetic stirring. Then, 0.1619 g NH_4F and 5 ml deionized water were added to the above mixed solution with 1.5-h stirring. After hydrothermal reaction at 180 °C for 12 h, the mixture was cooled to room temperature. The precipitates were collected via centrifugation, followed by washing and drying. As-prepared powders were further calcined at 500 °C for 5 h in muffle furnace to obtain (Ca,Y)F_2:Tm,Yb nanoparticles. TiO_2/(Ca,Y)F_2:Tm,Yb composite was prepared by a PVP-assisted surface coating [30] and hydrothermal crystallization method. In brief, 1 ml Hacac and 0.4 ml TTIP were added into 20 ml anhydrous ethanol, and acetic acid was added to adjust pH to 0.2 with 1-h stirring to prepare TTIP precursor solution. Next, 100 mg (Ca,Y)F_2:Tm,Yb was dispersed in 10 ml (0.02 g·ml^{-1}) PVP solution under ultrasonication to form a homogeneous white suspension. Subsequently, TTIP precursor solution was added to as-prepared white suspension with 2-h vigorous stirring, and the mixture was transferred to a Teflon-lined stainless steel autoclave and heated at 150 °C for 8 h to produce a crystalline TiO_2 shell. After cooling to room temperature, the resulting sample was obtained by centrifugation, washed with ultrapure water and ethanol, respectively, dried at 60 °C in oven. After being fully grounded, TiO_2/

$(Ca,Y)F_2$:Tm,Yb composite powders were heated at 400 °C for 5 h.

2.3 Synthesis of GO-TiO_2/$(Ca,Y)F_2$:Tm,Yb

As-prepared TiO_2/$(Ca,Y)F_2$:Tm,Yb was dispersed in 30 ml deionized water under ultrasonication followed by dropwise addition of GO solution ($1\ mg\cdot ml^{-1}$) under vigorous stirring for 2 h, in which the weight ratio of GO to TiO_2/$(Ca,Y)F_2$:Tm,Yb was set to 0%, 1%, 3% and 5%, respectively (Table 1). After stirring, the suspension was transferred to a Teflon-lined stainless steel autoclave and heated to 180 °C for 12 h. After cooling to room temperature, as-formed GO-TiO_2/$(Ca,Y)F_2$:Tm,Yb particles were collected by centrifugation, washed several times with deionized water/ethanol, and subsequently freeze-dried.

2.4 Characterization

The crystalline structure of prepared samples was tested by X-ray diffraction (XRD, Bruker D8 Discover, Cu Kα1 irradiation in 2θ range of 5°–90°. The morphologies and microstructures of samples were characterized using scanning electron microscopy (SEM, S-4800, Hitachi Limited) and X-ray photoelectron spectroscopy (XPS, ESCALAB 250Xi, Thermo Fisher Scientific). XPS measurements were performed on an ESCALAB 250Xi photoemission spectrometer using an Al Kα dual anode as source, aimed to determining the molecular structure, chemical valence state and elemental composition content of samples. In addition, Brunauer–Emmett–Teller (BET, Autosorb-iQ, Quantachrome) specific surface area and nitrogen adsorption–desorption isotherms of samples were analyzed with a Quanta chrome Autosorb-iQ-MP-XR system at 77 K.

Ultraviolet–visible (UV–Vis) diffuse reflectance spectra (UV–Vis DRS, Lambda 1500 +, PerkinElmer) of samples were obtained using a Lambda 1500 + UV–Vis spectrophotometer. ESR (JES-FA200, Business Guide-Sha, Japan) was used to test the electron–hole separation. Photoelectrochemical measurements of samples were performed using an electrochemical workstation (CHI 660E, Shanghai Chen Hua Instrument Company, China), a 300 W xenon lamp, a platinum net as counter electrode, Ag/AgCl as reference electrode and Na_2SO_4 ($0.1\ mol\cdot L^{-1}$) as electrolyte. The working electrode was prepared on indium tin oxide (ITO) conductive glass, which was cleaned by anhydrous ethanol and deionized water under ultrasonic conditions for 30 min. In brief, an appropriate amount of polyvinyl alcohol (PVA) was added to 1 ml deionized water, and an appropriate amount of sample (4:1) was added after PVA until it was fully dissolved. When the solution was stirred to form a paste, the above mixture was deposited onto ITO glass with areas of $\sim 1\ cm^2$. Frequency range of $0.05–1 \times 10^5$ Hz was set, and applied bias of 1.5 V band potential (VFB) was determined by Mott–Schottky plots from impedance spectra collected in the potential range from + 1 to − 0.2 V.

Table 1 Composition of experimental samples

GO content / wt%	TiO_2/$(Ca,Y)F_2$: Tm,Yb content / wt%	Sample
0	100	TiO_2/$(Ca,Y)F_2$:Tm,Yb
1	99	1%GO-TiO_2/$(Ca,Y)F_2$:Tm,Yb
3	97	3%GO-TiO_2/$(Ca,Y)F_2$:Tm,Yb
5	95	5%GO-TiO_2/$(Ca,Y)F_2$:Tm,Yb

2.5 Photocatalytic activity evaluation

The photocatalytic activity of GO-TiO_2/$(Ca,Y)F_2$:Tm,Yb samples for organic pollutant degradation was evaluated using photocatalytic discoloration of MO. 50 mg photocatalyst was suspended in 50 ml MO ($15\ mg\cdot L^{-1}$) aqueous solution to form a homogenous suspension. The suspension was stirred in a dark environment for 30 min to achieve adsorption/desorption equilibrium. Next, the suspensions were irradiated using a 300 W xenon lamp. After irradiation for 120 min, 3 ml pollutant aqueous suspension was removed and centrifuged. The resulting supernatants were used to perform UV–Vis absorbance measurements at 464 nm for MO. The degradation rate of MO in an organic solvent is calculated as follows:

$$\eta = \frac{(C_0 - C_t)}{C_0} \times 100\% \tag{1}$$

where η is the degradation rate of MO, C_t is the concentration of pollutants at irradiation time (t), and C_0 is the concentration of the photocatalysts in absorption equilibrium before irradiation.

Besides, the stability of nanocomposites was examined by studying its reusability in a four successive runs. At the end of each experiment, the photocatalyst used in the experiment was collected, washed with ultrapure water and ethanol, respectively, dried at 60 °C in an oven for 24 h. The treated material was then used in a new round of experiment. The degradation effect of MO by GO-TiO_2/$(Ca,Y)F_2$:Tm,Yb under different light sources was evaluated by the photocatalytic discoloration as mentioned above. A filter plate was placed under the xenon lamp light source to screen out ultraviolet visible light and near-infrared light for testing the influence of different light sources on the degradation effect. In the same way, 10, 20, 30, 50 and 100 mg 3%GO-TiO_2/(Ca,Y)F_2:Tm,Yb were added to the beaker to conduct MO degradation experiment, respectively, so as to test the influence of photocatalyst amount on the catalytic effect.

The photocatalytic activity of the materials was determined by electron spin resonance spectrometer (ERS). Dimethyl sulfoxide (DMSO) was used as a trapping agent to detect ·OH produced by the composite photocatalyst. 1,3-Diphenylisobenzofuran (DPBF) was used to capture $\cdot O_2^-$.

2.6 Antibacterial activity measurements

The antibacterial potential of GO-TiO_2/(Ca,Y)F_2:Tm,Yb composite photocatalyst was evaluated according to GB/T2 1510–2008 “the antibacterial performance test of nano inorganic materials”. Gram-negative *E. coli* and Gram-positive *S. aureus* were used as model bacterial to assess samples photocatalytic antibacterial activity. 2 ml bacterial suspension (1×10^7 CFU·ml^{-1}) was mixed with 2 mg photocatalyst, followed by 500 W xenon lamp exposure for 2 h. Next, 100 μl suspension (diluted 10, 100 and 1000 times, two replicates) was uniformly coated on agar plates of solid medium and cultured at 37 °C for 12 h for standard bacterial colony counting. Catalysts without light exposure were used as control. In addition, bacterial live/dead fluorescence test was also conducted. The bacterial suspension was mixed with TiO_2/(Ca,Y)F_2:Tm,Yb to form a coculture solution with a final concentration of 500 μg·ml^{-1}, which was irradiated with light for 120 min. Next, the bacteria were stained with SYTO9 (Thermo Fisher, Shanghai, China) and PI fluorescent dye reagents (Thermo Fisher, Shanghai, China), and the cell live/dead status was detected by fluorescence microscopy (TCS SP4, Leica, Germany). For each material, three sets of parallel experiments were set up to calculate the antibacterial rate and error. The bacterial inhibition rate was calculated as follows:

$$R = \frac{B - S}{B} \tag{2}$$

where R stands for antibacterial rate, B and S stand for colony number of blank control and test groups, respectively.

3 Results and discussion

3.1 Morphology and structure

The crystal structure of the photocatalytic composite material prepared experimentally was analyzed by XRD, and the obtained patterns are shown in Fig. 1a. XRD pattern of TiO_2/(Ca,Y)F_2:Tm,Yb shows obvious diffraction peaks at $2\theta = 25.3°$, 37.8°, 48.0°, 53.9°, 62.7° and 75.1°, corresponding to the (101), (004), (200), (105), (204) and (215) reflection planes of cubic TiO_2 (PDF No. 71–1166), respectively. Besides, characteristic peaks at $2\theta = 28.1°$, 32.5°, 46.7° and 55.4° can be assigned to the (111), (200), (220) and (311) reflection planes of (Ca,Y)F_2 (PDF No. 31–0293), respectively. The concentrations of Tm and Yb were too low to cause no significant impact on the phase purity of TiO_2/(Ca,Y)F_2:Tm,Yb [31]. On the other hand, similar XRD patterns between TiO_2/(Ca,Y)F_2:Tm,Yb and GO-TiO_2/(Ca,Y)F_2:Tm,Yb samples indicates that GO has no significant impact on the phase purity of TiO_2/(Ca,Y)F_2:Tm,Yb. In addition, a characteristic peak of GO at 11° in GO/ TiO_2/(Ca,Y)F_2:Tm,Yb samples is absent, attributed to the low content of GO [32, 33]. In Fig. 1b, typical GO appears as a sheet structure. As shown in Fig. 1c, d, TiO_2/(Ca,Y)F_2:Tm,Yb nanoparticles are distributed on GO surface after hydrothermal reaction. The large specific surface area of GO can offer a platform for uniform growth of TiO_2, effectively inhibiting its agglomeration [34].

XPS result is shown in Fig. 2a–d. Comprehensive energy spectrum of 3% Go-TiO_2/(Ca,Y)F_2:Tm,Yb composite materials is shown in Fig. 2a, in which five binding energy peaks observed at 457.98, 529.3, 283.76, 684.78 and 384.11 eV are attributed to Ti 2p, O 1s, C 1s, F 1s and Ca 2p, respectively. In Fig. 2b, peaks at 459.95 and 465.6 eV can be assigned to Ti $2p_{3/2}$ and Ti $2p_{1/2}$, respectively. The calculated energy gap difference between the two peaks is 5.65 eV, indicating the presence of Ti^{4+} [35] in the Ti–O composites. There are four peaks belonging to C 1s XPS spectra of GO-TiO_2/(Ca,Y)F_2:Tm,Yb (Fig. 2c), in which peak at 284.5 eV is due to sp2 hybridized (C=C) double bonds, and peaks observed at 285.82, 287.2 and 289.85 eV correspond to C–OH, C-O and O-C=O bonds, respectively [36]. Compared with pure GO, the C=O absorption peak strength of GO-TiO_2/(Ca,Y)F_2:Tm,Yb composites is relatively weak, indicating that GO as well as its C=O content is reduced during the hydrothermal preparation of composites [37]. In addition, the O 1s energy spectrum in Fig. 2d shows three peaks at 530.83, 531.3 and 533 eV, contributed to Ti–O, Ti–OH and C–OH, respectively. Therefore, TiO_2 is successfully loaded onto the surface of GO through chemical bond connections, providing an interface for electron transfer between TiO_2 and GO.

The specific surface area was investigated using BET gas adsorption measurements. Nitrogen (N_2) adsorption–desorption isotherms were obtained to demonstrate the specific surface area, pore size and relative textural properties of the TiO_2/(Ca,Y)F_2:Tm,Yb, 1%, 3% and

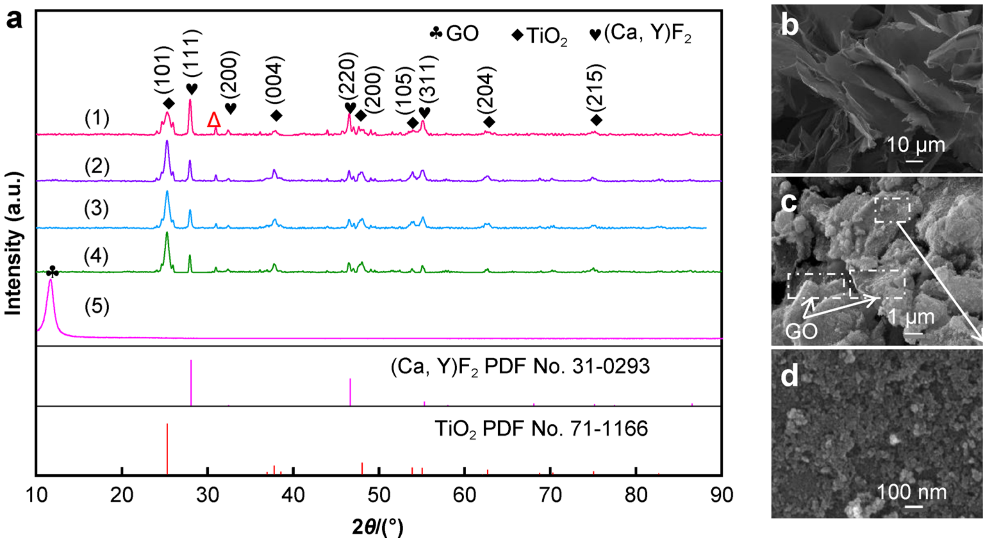

Fig. 1 **a** XRD patterns of (1) $TiO_2/(Ca,Y)F_2$:Tm,Yb, (2) 1%GO-$TiO_2/(Ca,Y)F_2$:Tm,Yb, (3) 3%GO-$TiO_2/(Ca,Y)F_2$:Tm,Yb, (4) 5%GO-$TiO_2/(Ca,Y)F_2$:Tm,Yb and (5) GO; **b** SEM images of GO and **c-d** low- and high-magnification SEM images of 3%GO-$TiO_2/(Ca,Y)F_2$:Tm,Yb

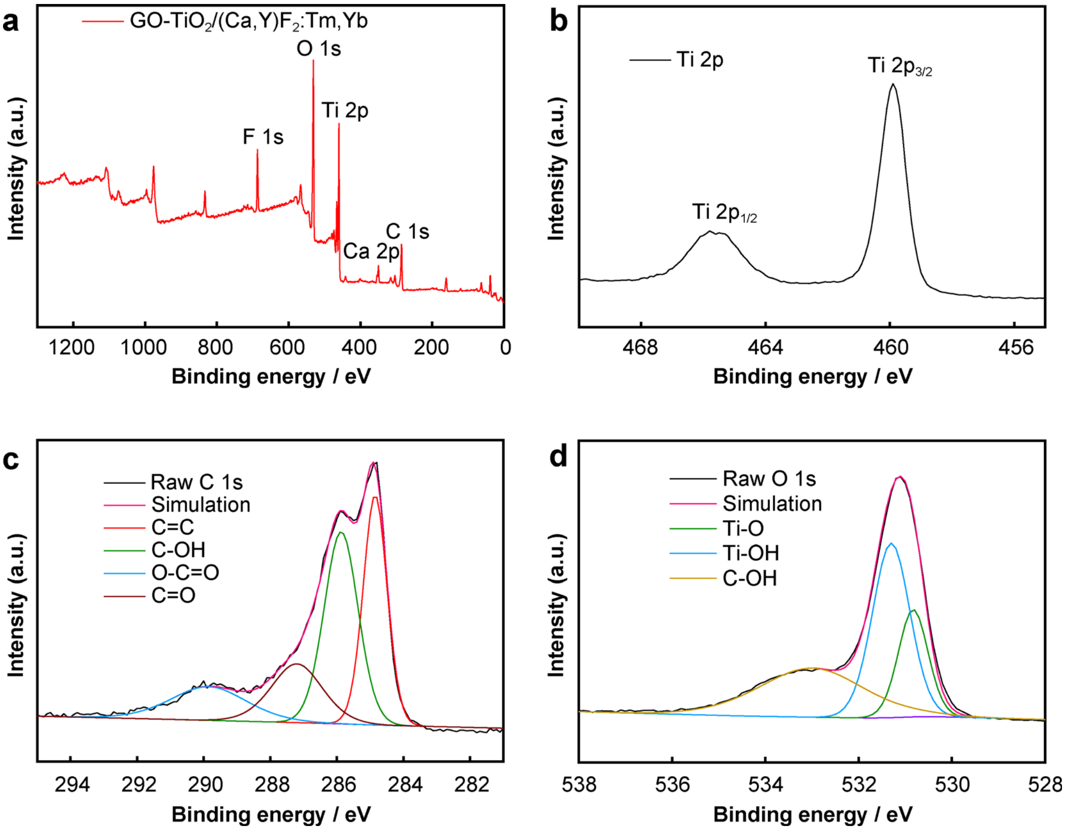

Fig. 2 **a** XPS survey spectra, **b** Ti 2p, **c** C 1s and **d** O 1s XPS spectra of 3%GO-$TiO_2/(Ca,Y)F_2$:Tm,Yb composite material

5%GO-$TiO_2/(Ca,Y)F_2$:Tm,Yb nanocomposites at 377 K using multipoint BET method. As shown in Fig. 3a, all isotherms show a typical H_3 hysteresis loop shape. According to the Brunauer–Deming–Deming–Teller classification, the existence of corresponding mesopores (2–50 nm) can be confirmed. Figure 3b depicts the pore size distribution curves of the $TiO_2/(Ca,Y)F_2$:Tm,Yb and 1%, 3% and 5%GO-$TiO_2/(Ca,Y)F_2$:Tm,Yb composites.

The obtained surface area and pore volume of TiO_2/(Ca,Y)F_2:Tm,Yb are 40.221 $m^2 \cdot g^{-1}$ and 0.299 $cm^3 \cdot g^{-1}$, respectively. After GO was combined into the composite material, the obtained surface areas of 1%, 3% and 5%GO-TiO_2/(Ca,Y)F_2:Tm,Yb are 59.148, 63.835 and 66.652 $m^2 \cdot g^{-1}$, respectively. Besides, the pore volumes of 1%, 3% and 5%GO-TiO_2/(Ca,Y)F_2:Tm,Yb are 0.255, 0.215 and 0.246 $cm^3 \cdot g^{-1}$, respectively. With an increase in material specific surface area, adsorption of pollutants to photocatalyst surface is expected to increase, further enhancing photocatalytic degradation. In addition, the increase in specific surface area is primarily due to the introduction of GO on the surface of the nanocomposites, indicating that the addition of GO can provide more surface sites to accommodate more adsorbed drug pollutants, which is beneficial for photocatalysis.

3.2 Optical property studies

UV−Vis absorption spectroscopy was used to investigate the optical properties of the prepared nanocomposites. The result is shown in Fig. 4. The optical properties of TiO_2/(Ca,Y)F_2:Tm,Yb nanocomposites were significantly affected by the addition of GO at different weight ratios. Figure 4 shows that the peaks observed at 404 nm correspond to a band gap of 3.18 eV. Figure 4a clearly reveals that GO significantly enhances the absorption properties of the catalyst in the visible light region. Therefore, with GO content increasing, the absorption peak moves to a higher wavelength, which eventually leads to a decrease in the band gap energy. Figure 4b shows that the increase in GO content decreases the band gap of TiO_2/(Ca,Y)F_2:Tm,Yb from 3.18 to 2.88 eV (1%GO-TiO_2/(Ca,Y)F_2:Tm,Yb), 2.65 eV (3%GO-TiO_2/(Ca,Y)F_2:Tm,Yb) and 2.94 eV (5%GO-TiO_2/(Ca,Y)F_2:Tm,Yb). TiO_2 composite material, with a smaller band gap energy, shows better photocatalytic activity. The decrease in band gap energy can be attributed to the chemical bonding between TiO_2/(Ca,Y)F_2:Tm,Yb and GO [38]. In addition, the band gap of TiO_2 decreases with GO content increasing, confirming that charge delocalization is caused by strong chemical bonding between the carbon at a specific location in GO and the semiconductor [39, 40].

3.3 Photoelectrochemical measurements

The interfacial charge separation efficiency of the composite photocatalyst was examined using electrochemical impedance (EIS) spectra. Figure 5 shows EIS Nyquist plots of TiO_2/(Ca,Y)F_2:Tm,Yb and GO-TiO_2/(Ca,Y)F_2:Tm,Yb samples. The arc radius of the EIS Nyquist curve can reflect the reaction rate on the electrode surface. The smaller the arc radius is, the more effective the separation of photogenerated electron–hole pairs is, and the higher the charge migration efficiency through the electrode/electrolyte interface is. As can be seen, the arc radius of GO-TiO_2/(Ca,Y)F_2:Tm,Yb is significantly smaller than that of TiO_2/(Ca,Y)F_2:Tm,Yb, indicating that the separation and migration of the photoelectron–hole pair at the GO-TiO_2/(Ca,Y)F_2:Tm,Yb electrode are more effective. This phenomenon further confirms that the presence of GO can promote charge separation of the photoelectron–hole pair at the interface. However, the Nyquist arc radius of the composite photocatalyst with 5% GO is larger than that of TiO_2/(Ca,Y)F_2:Tm,Yb, which may be caused by excessive GO used as the recombination center of photogenerated carriers. In addition, the smallest arc radius of EIS Nyquist curve belongs to composite photocatalyst with 3% GO addition, suggesting that it is the most effective formula for separation of photogenerated electron and hole pairs.

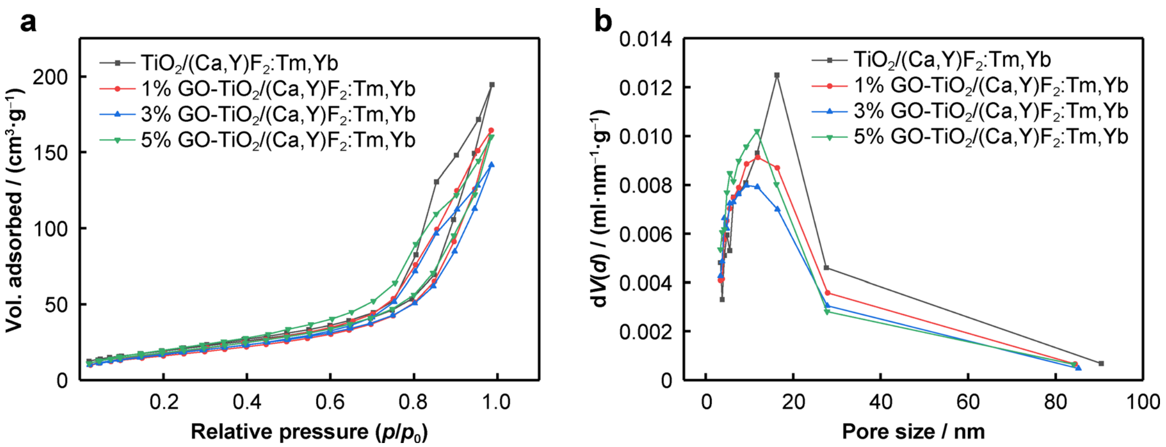

Fig. 3 **a** N_2 adsorption–desorption isotherms of TiO_2/(Ca,Y)F_2:Tm,Yb and 1%, 3%, 5%GO-TiO_2/(Ca,Y)F_2:Tm,Yb; **b** pore size distribution curves of TiO_2/(Ca,Y)F_2:Tm,Yb and 1%, 3%, 5%GO-TiO_2/(Ca,Y)F_2:Tm,Yb

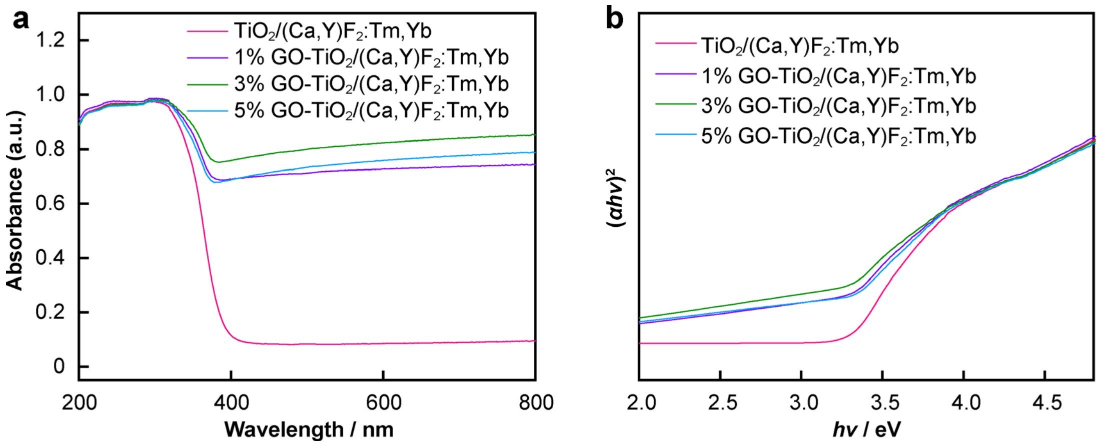

Fig. 4 **a** UV–Vis diffuse reflectance absorption; **b** diffuse reflectance determination spectra of $TiO_2/(Ca,Y)F_2$:Tm,Yb, 1%, 3% and 5%GO-$TiO_2/(Ca,Y)F_2$:Tm,Yb

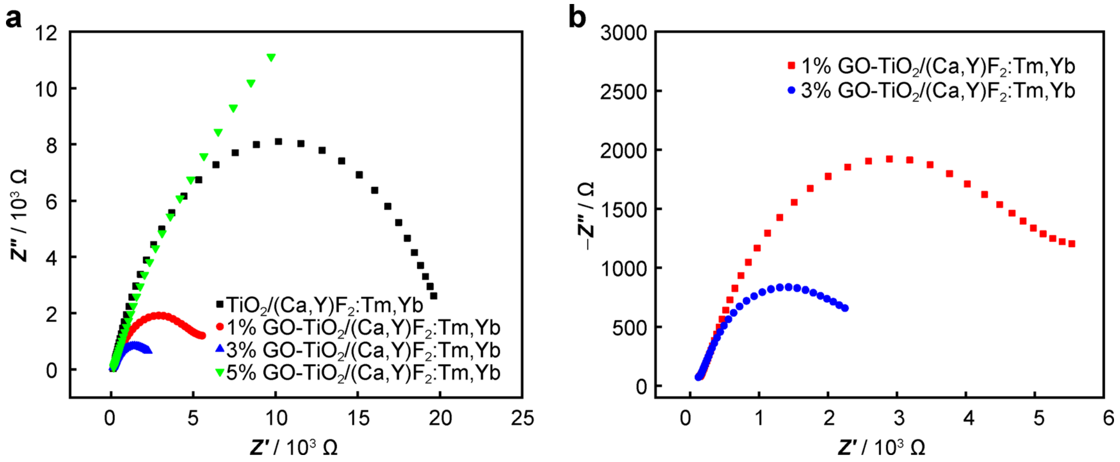

Fig. 5 **a** EIS Nyquist plots of $TiO_2/(Ca,Y)F_2$:Tm,Yb and GO-$TiO_2/(Ca,Y)F_2$:Tm,Yb in a 0.1 mol·L^{-1} Na_2SO_4 solution; **b** EIS Nyquist plots of 1%GO-$TiO_2/(Ca,Y)F_2$:Tm,Yb and 3%GO-$TiO_2/(Ca,Y)F_2$:Tm,Yb in a 0.1 mol·L^{-1} Na_2SO_4 solution

3.4 Adsorption and photocatalytic activity studies

The large surface area of GO is beneficial for adsorbing more pollutants. In this work, MO is a water-soluble azo dye that almost does not degrade itself under sunlight irradiation. It is a typical dye in wastewater and has been used as an organic pollutant model for adsorption and photocatalytic activity tests.

To estimate the adsorption of MO by as-prepared photocatalysts, dark adsorption experiments were performed by stirring in the dark for 30 min before irradiation. Each material can reach adsorption equilibrium within 30 min (Fig. 6a). The adsorption removal rates of TiO_2/ $(Ca,Y)F_2$:Tm,Yb within 30 min were 1.33%. On contrast, the adsorption removal rates of 1 wt%, 3 wt% and 5 wt%GO-$TiO_2/(Ca,Y)F_2$:Tm,Yb were 20.21%, 39.21% and 44.02%, respectively. Owing to non-covalent heterotopic interactions, MO with aromatic rings can be adsorbed on the two-dimensional nanosheets of GO, displaying a GO content dependent MO adsorption behavior. It is known that photocatalytic redox reaction usually occurs on the surface of the photocatalyst; therefore, adsorption of dye molecules is a prerequisite for following photocatalytic degradation of dyes [33]. Therefore, enhanced dye adsorption by GO is expected to improve the photocatalytic degradation activity of $TiO_2/(Ca,Y)F_2$:Tm,Yb.

Under full spectral irradiation, the photocatalytic degradation of MO by $TiO_2/(Ca,Y)F_2$:Tm,Yb and GO-$TiO_2/(Ca,Y)F_2$:Tm,Yb changes with time. After 120 min simulated sunlight irradiation using 300 W xenon lamp, $(Ca,Y)F_2$:Tm,Yb almost did not degrade MO, and the degradation rate of MO by $TiO_2/(Ca,Y)F_2$:Tm,Yb was 57.02%, attributed to the photocatalytic ability of the semiconductor TiO_2. For the aspect of GO-TiO_2/ $(Ca,Y)F_2$:Tm,Yb, the photocatalytic performance largely depends on the content of GO in the catalyst. As shown in Fig. 6b, after the introduction of GO, the degradation rates of MO by 1%, 3% and 5%GO-$TiO_2/(Ca,Y)F_2$:Tm,Yb

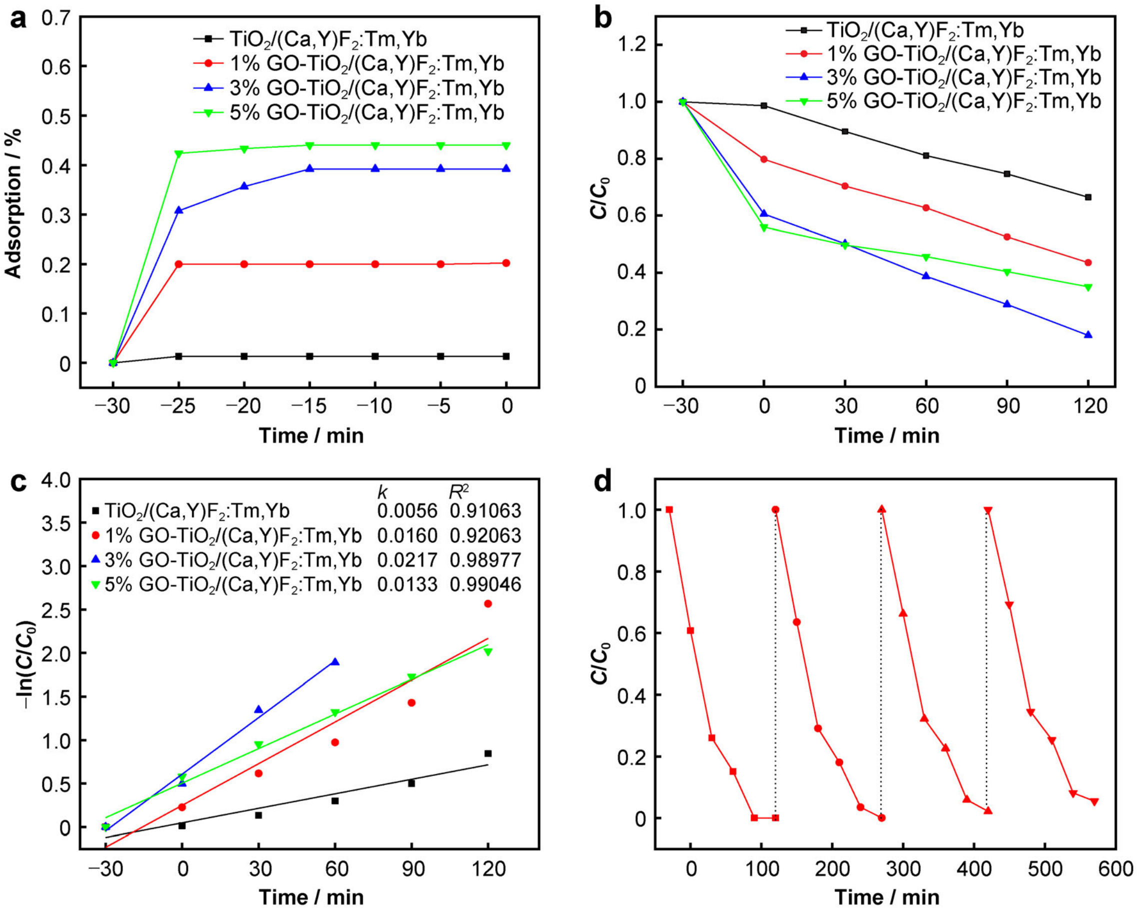

Fig. 6 **a** Removal rate in dark reaction; **b** residual concentration ratio of MO under full-spectrum irradiation; **c** kinetic curves of MO degradation under full-spectrum irradiation; **d** recycling tests of 3%GO-TiO_2/(Ca,Y)F_2:Tm,Yb for methyl orange degradation

increase to 92.32%, 100% and 86.75%, respectively. In addition, as an electron flow conductor, GO improves the energy transfer between up-conversion luminescent materials and TiO_2, thereby improving the photocatalytic activity of TiO_2. Although 5 wt% GO-TiO_2/(Ca,Y)F_2:Tm,Yb has the highest adsorption capacity, its photocatalytic degradation of MO is not the best, which may be caused by following factors: (1) a large amount of GO could shield TiO_2 from the incident light, which significantly affected the excitation of the carrier [41, 42]; (2) excessive GO, as the recombination center of photogenerated carriers, could lead to a decrease in photocatalytic activity [43]; (3) excessive GO absorbed excessive near-infrared light, which limited the luminescence of (Ca,Y)F_2:Tm,Yb up-conversion.

To further quantitatively evaluate the photocatalytic efficiency of TiO_2/(Ca,Y)F_2:Tm,Yb and 1%, 3% and 5%GO-TiO_2/(Ca,Y)F_2:Tm,Yb composite photocatalysts, pseudo-first-order dynamics model [44] was applied to evaluate the photocatalytic degradation rate (Eq. (3)). Figure 6c shows the linear relationship between $\ln(C/C_0)$ and irradiation time (t). In addition, the apparent degradation rate constant (k) can be calculated by plotting $\ln(C/C_0)$ versus irradiation time. All experimental data fit the first-order kinetic model well. At the same time, the incorporation of GO into TiO_2/(Ca,Y)F_2:Tm,Yb significantly promotes the degradation rate of organic pollutants. The k values of TiO_2/(Ca,Y)F_2:Tm,Yb, 1%GO-TiO_2/(Ca,Y)F_2:Tm,Yb, 3%GO-TiO_2/(Ca,Y)F_2:Tm,Yb and 5%GO-TiO_2/(Ca,Y)F_2:Tm,Yb are 0.0056, 0.016, 0.0217 and 0.0133, respectively. The analytical results are in agreement with experimental results, in which 3%GO-TiO_2/(Ca,Y)F_2:Tm,Yb photocatalysts shows better catalytic activity. The pseudo-first-order dynamics model equation is as follows:

$$\ln\frac{C}{C_0} = -kt \quad (3)$$

where C is the residual concentration of MO at time t (mg·L^{-1}), and C_0 is the initial concentration of MO (mg·L^{-1}). The apparent rate constant (min^{-1}) and reaction time (min) of MO are expressed by k and t, respectively.

In addition to photocatalytic efficiency, photocatalytic stability of catalyst also plays an important role in practice.

To further investigate the photocatalytic stability of 3%GO-TiO_2/(Ca,Y)F_2:Tm,Yb composite photocatalyst, a four successive runs photocatalytic degradation test was performed. As can be seen from Fig. 6d, after four successive runs, efficiency of GO-TiO_2/(Ca,Y)F_2:Tm,Yb for photocatalytic degradation of MO decreases from 100% to 94.54%. This efficiency loss may be caused by the centrifugation, drying or recovery step of the catalyst in the recycling process. In summary, the prepared photocatalyst has high working stability and efficient recovery performance [45].

Results of photocatalytic degradation of MO by the composite photocatalyst under irradiation by different light sources are shown in Fig. 7. In Fig. 7a-c, under UV light, degradation efficiencies of MO by TiO_2/(Ca,Y)F_2:Tm,Yb and 1%, 3% and 5%GO-TiO_2/(Ca,Y)F_2:Tm,Yb within 120 min are 32.45%, 100%, 94.86% and 70.44%, respectively. Under visible light irradiation, degradation rates of the four photocatalyst samples are 12.99%, 60.67%, 83.51% and 63.75%, respectively. Under NIR light irradiation, the degradation rates of 33.55%, 56.46%, 82.05% and 64.93% are achieved for the composite photocatalyst samples. These results show that GO-TiO_2/(Ca,Y)F_2:Tm,Yb composite photocatalysts display different responses to light sources in different wavelength ranges, in which 1%GO-TiO_2/(Ca,Y)F_2:Tm,Yb, 3%GO-TiO_2/(Ca,Y)F_2:Tm,Yb and 3%GO-TiO_2/(Ca,Y)F_2:Tm,Yb exhibit the best response to UV, visible and NIR light, respectively. Figure 7d−f shows that removal of MO by photocatalyst fits the first-order kinetic model well (Eq. (3)). The degradation rate constants of the photocatalysts under UV light are slightly higher than those under visible light and NIR light, revealing that UV light remains the main light source responsible for the photocatalytic behavior of TiO_2. This is particularly evident in the composite photocatalyst doped with 1% GO. TiO_2/(Ca,Y)F_2:Tm,Yb materials mainly absorb UV light and have limited ability to absorb visible light. Therefore, TiO_2/(Ca,Y)F_2:Tm,Yb has the poorest degradation effect on MO under visible light irradiation. The NIR photothermal effect is stronger than UV light and visible light. When NIR light is used for catalytic reaction, the temperature and degradation rate of MO solution will increase relatively, thus producing the degradation effect comparable to that under UV light irradiation. In general, the photocatalytic activity of GO-TiO_2/(Ca,Y)F_2:Tm,Yb is better than that of TiO_2/(Ca,Y)F_2:Tm,Yb under irradiation by different light sources because TiO_2 interacts with the conjugated π bonds on the GO surface. Under the excitation of light, the photogenerated holes in the TiO_2 valence band can be accelerated to the GO surface, which promotes the separation of holes and electrons. At the same time, the

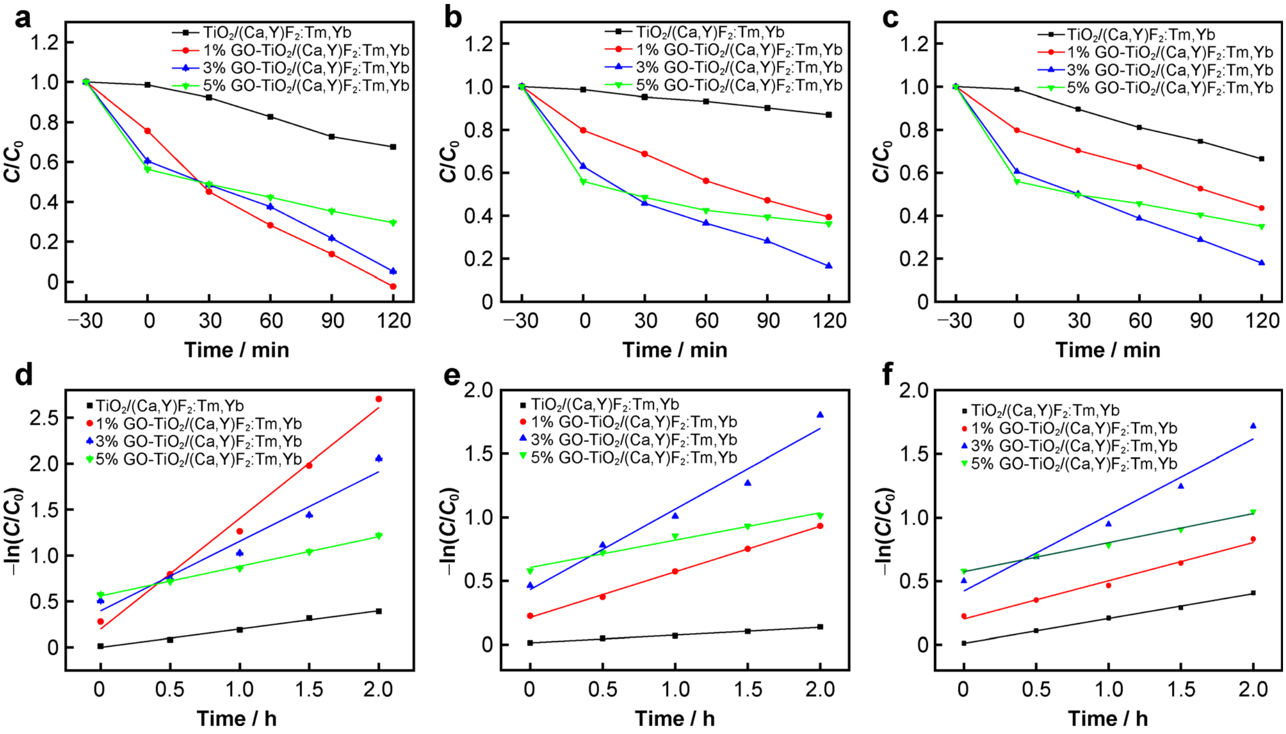

Fig. 7 Photocatalytic degradation of MO by composite photocatalysts under irradiation by different light sources and kinetic linear fitting analysis: **a** UV light; **b** visible light; **c** near-infrared light; **d-f** degradation kinetics curves of MO under UV light, visible light and near-infrared light

photogenerated holes transferred to the GO surface can directly oxidize with the organic pollutants adsorbed on the surface of the catalyst, thereby improving the degradation efficiency. But excessive doping of GO will lead to the formation of recombination center, which is unfavorable to the separation of photogenerated charges and consequently, reduces associated photocatalytic activity of the catalyst. In addition, temperature is also believed to have a certain impact on the degradation rate of MO. Owing to the limitation of experimental conditions, it is hard to determine the effect of temperature change on MO degradation caused by sample under irradiation alone.

The effects of different amounts of catalyst on the degradation of MO were further studied. The initial concentration of MO was 15 mg·L^{-1}, and the amount of catalyst was 10, 20, 30, 50 and 100 mg. The test results are shown in Fig. 8. In the dark reaction stage, MO removal rate of the 3%GO-TiO_2/(Ca,Y)F_2:Tm,Yb composite material increased with catalyst content increasing, induced by adsorption of MO to catalyst surface. A xenon lamp was used immediately after the end of the dark reaction to start the photocatalytic reaction. The degradation rates of MO by five different catalyst amounts after 120 min were 21.73%, 67.17%, 93.15%, 100% and 100%, respectively, revealing a catalyst concentration dependent MO degradation behavior. During the whole reaction process, the MO removal rate generally increased with the increase in the amount of composite photocatalyst.

To verify antibacterial properties of the composite photocatalyst, two kinds of bacteria were selected as representative models: *Staphylococcus aureus (S. aureus)* and *Escherichia coli* (*E. coli)*. As shown in Fig. 9a, c, after 120-min irradiation under light, the antibacterial rates of TiO_2/(Ca,Y)F_2:Tm,Yb against *S. aureus* and *E. coli* reach 89.1% ± 1.1% and 91.3% ± 0.8%, respectively. At the same dose, the antibacterial rates of 3%GO-TiO_2/(Ca,Y)F_2:Tm,Yb against *S. aureus* and *E. coli* are 96.4% ± 1.6% and 94.8% ± 0.4%, respectively. As shown in Fig. 9b, d, only a small number of dead bacteria associated red fluorescent spots can be seen in the fluorescence images of control group, showing that light cannot kill bacteria. In group of photocatalyst, large areas of red fluorescence appear on contrast. In addition, 3%GO-TiO_2/(Ca,Y)F_2:Tm,Yb shows better antibacterial ability than TiO_2/(Ca,Y)F_2:Tm,Yb. These results are in accordance with the plate counting results, revealing the advantage of photocatalysts in *E. coli* and *S. aureus* elimination under full spectrum sun light. Besides, TiO_2/(Ca,Y)F_2:Tm,Yb and 3%GO-TiO_2/(Ca,Y)F_2:Tm,Yb in darkness exhibit limited bacteria inhibitory effect. This is due to the fact that rare earth ions have certain antibacterial properties [46]. The rare earth ions (Y^{3+}, Tm^{3+} and Yb^{3+}) in the material may react with peptidoglycan and lipopolysaccharide in the bacterial structure, causing bacterial cell structure damage. In addition, rare earth ions may also inhibit the activity and synthesis of various enzymes in bacterial cells, thus affecting the proliferation and growth of bacteria [47, 48].

3.5 Mechanisms of photocatalytic activity

ESR was used to study the photoactive substances produced by photocatalysts in photocatalysis (Fig. 10). After the introduction of GO, the ESR signal intensity increases. The presence of GO can promote h^+–e^- separation, prompting more h^+–e^- pairs to reach the particle surface and water to generate ·OH and $·O_2^-$ for photocatalytic activity enhancement. Therefore, MO degradation can be contributed to strong organic matter adsorption capacity of GO as well as its unique surface property. The former is caused by the high surface area of GO, which consequently enhances direct contact between TiO_2 and organic matter for photocatalytic efficiency improvement. The latter is

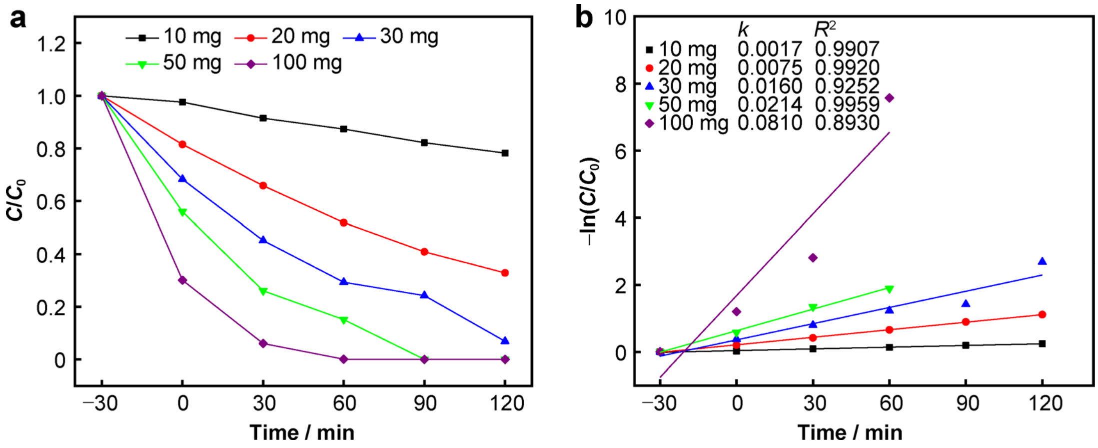

Fig. 8 **a** Residual concentration ratio and **b** kinetics plots showing linear fitting of data for MO degradation with respect to catalyst amount

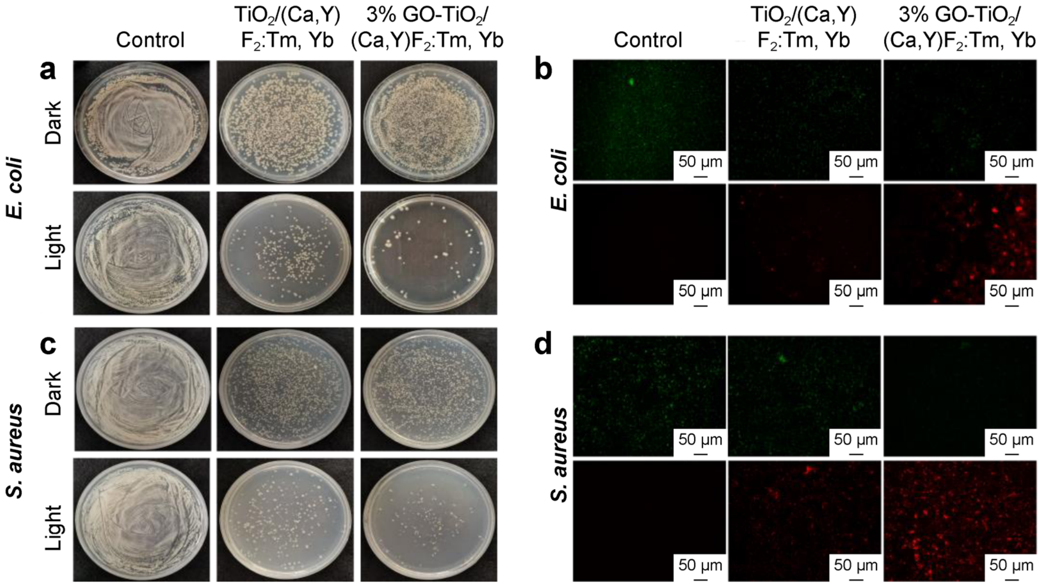

Fig. 9 Statistics of antibacterial activity of composite photocatalyst against **a** Gram-negative *E. coli* and **c** Gram-positive *S. aureus*; fluorescence images of bacteria stained by **b** *E. coli* and **d** *S. aureus* after composite photocatalyst treatment

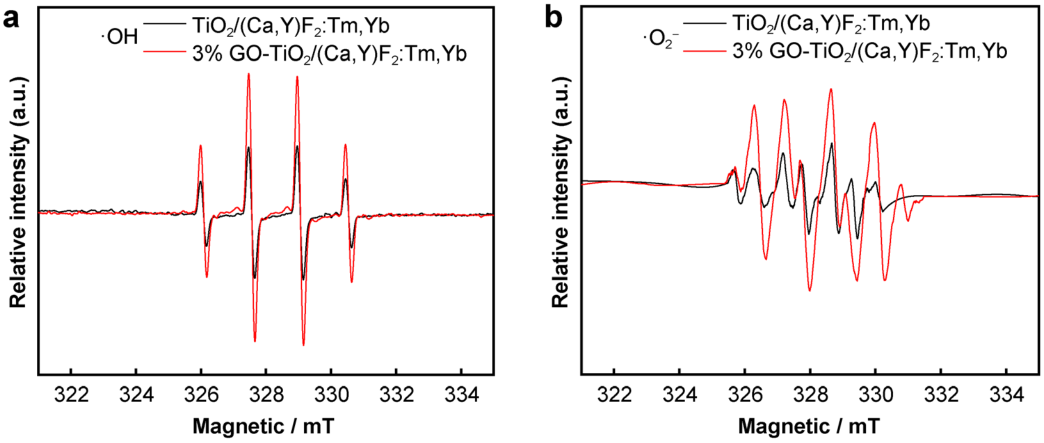

Fig. 10 ESR spectra of **a** ·OH and **b** $\cdot O_2^-$ signals of TiO_2/(Ca,Y)F_2:Tm,Yb and 3% GO-TiO_2/(Ca,Y)F_2:Tm,Yb photocatalysts at room temperature

contributed to the electrostatic repulsion property of GO surface, which enables TiO_2 excitation generated h^+–e^- free move and effectively separate the photogenerated electron–hole pairs to inhibit the recombination of photogenerated carriers.

Based on the above experimental results, the photocatalytic mechanism of GO-TiO_2/(Ca,Y)F_2:Tm,Yb composites is as follows: under full-spectrum irradiation, (Ca,Y)F_2:Tm,Yb, as a sensitizer, has a large absorption cross section for irradiation by near-infrared light and can be effectively excited from $^2F_{5/2}$ to $^2F_{7/2}$, and three successive energy transfers from Yb to Tm absorbs photon energy, resulting in $^1G_4 \rightarrow {}^3F_4$, $^1G_4 \rightarrow {}^3H_6$ and $^1I_6 \rightarrow {}^3H_6$ energy level transitions and emitting corresponding red light (650 nm), visible light (477 nm) and UV light (360 nm), respectively. The UV light (360 nm), visible blue light (477 nm) and red light (650 nm) emitted by the energy level transition can effectively excite TiO_2 to produce oxidation valence band holes (h^+) and reduction conduction band electrons (e^-). Photogenerated electron–hole pairs are separated and migrate to the ion surface under the action of an electric field. Photogenerated holes are highly oxidizing and can react with H_2O and OH^- adsorbed on the surface of TiO_2 to generate a hydroxyl radical (·OH). The electrons generated by the transition react with the oxygen adsorbed on TiO_2 surface to form a superoxide ion $\cdot O_2^-$, which can partially undergo a chain reaction to form ·OH. The hydroxyl and superoxide ions generated on the surface of TiO_2 have strong oxidizing properties capable of breaking the chemical bonds to organics, thereby enabling those small organic molecules to be oxidized into carbon dioxide and water. In addition, due to the interaction between GO and TiO_2, the photogenerated holes will transfer to GO, which will slow down the recombination of holes and electrons and thus, improve the photocatalytic efficiency. Moreover, porous GO can act as an adsorbent, making it easier for the holes to react with organic matter.

4 Conclusion

In this work, GO-TiO_2/(Ca,Y)F_2:Tm,Yb photocatalyst nanocomposites with different mass ratios of GO were developed. The photocatalytic degradation of the organic pollutant MO and the significant antibacterial effect toward *E. coli* and *S. aureus* were achieved by using GO-TiO_2/(Ca,Y)F_2:Tm,Yb nanocomposites as photocatalysts under simulated sunlight full-spectrum irradiation. Under full spectral light irradiation, 3%TiO_2/(Ca,Y)F_2:Tm,Yb material has the highest degradation rate (100%) of MO within 120 min, which was about 40% higher than that of TiO_2/(Ca,Y)F_2:Tm,Yb. At the same time, the antibacterial rate against *S. aureus* and *E. coli* within 120 min was 96.4% ± 1.6% and 94.8% ± 0.4%, respectively, higher than that of TiO_2/(Ca,Y)F_2:Tm,Yb. The composite material has a wider absorption spectrum, in which UV light is still the main excitation source of TiO_2. On this basis, different mechanisms of photocatalytic activity enhancement were discussed. The large specific surface area of GO helps to reduce the agglomeration of nanomaterials. The photoelectron–hole pairs generated by TiO_2 excited can move freely to the surface of GO, which effectively separates the photoelectron–hole pairs and inhibits the recombination of photogenerated carriers. More photogenerated hole–electrons can reach the surface of the sample and react with water to form $\cdot OH$ and $\cdot O_2^-$ for photocatalytic performance improvement. Taken together, combination of GO and the up-conversion material with TiO_2 synergistically improves the adsorption capacity, photocatalytic activity and light absorption range of the composites.

Acknowledgements This work was financially supported by the National Key Research and Development Program of China (No. 2020YFC1107403), the National Natural Science Foundation of China (No. 51771069) and the Natural Science Foundation of Hebei Province of China (No. E2020202028).

Declarations

Conflict of interests The authors declare that they have no conflict of interests.

References

[1] Kumar SG, Devi LG. Review on modified TiO_2 photocatalysis under UV/visible light: selected results and related mechanisms on interfacial charge carrier transfer dynamics. J Phys Chem A. 2011;115(46):13211.

[2] Hashimoto K, Irie H, Fujishima A. TiO_2 photocatalysis: a historical overview and future prospects. Jpn J Appl Phys. 2005; 44(12R):8269.

[3] Pipi A, Byzynski G, Ruotolo L. Photocatalytic activity and RNO dye degradation of nitrogen-doped TiO_2 prepared by ionothermal synthesis. Mater Res. 2017;20(3):628.

[4] Katoueizadeh E, Zebarjad SM, Janghorban K. Optimization of synthesis conditions of N-doped TiO_2 nanoparticles using Taguchi robust design. Mater Chem Phys. 2017;201:69.

[5] Arabzadeh A, Salimi A. One dimensional CdS nanowire@ TiO_2 nanoparticles core-shell as high performance photocatalyst for fast degradation of dye pollutants under visible and sunlight irradiation. J Colloid Interf Sci. 2016;479:43.

[6] Lin ZJ, Wu SL, Liu XY, Qian S, Chu PK, Zheng YF, Cheung KM, Zhao Y, Yeung KW. A surface-engineered multifunctional TiO_2 based nano-layer simultaneously elevates the corrosion resistance, osteoconductivity and antimicrobial property of a magnesium alloy. Acta Biomater. 2019;99:495.

[7] Ren YW, Han YJ, Li ZY, Liu XM, Zhu SL, Liang YQ, Yeung KWK, Wu SL. Ce and Er co-doped TiO_2 for rapid bacteria-killing using visible light. Bioact Mater. 2020;5(2):201.

[8] Wang R, Tang T, Wei YC, Dang D, Huang KB, Chen XW, Yin H, Tao XQ, Lin Z, Lu GN. Photocatalytic debromination of polybrominated diphenyl ethers (PBDEs) on metal doped TiO_2 nanocomposites: mechanisms and pathways. Environ Int. 2019; 127:5.

[9] Guo F, Jia J, Dai D, Gao HT. The electronic properties and enhanced photocatalytic mechanism of TiO_2 hybridized with MoS_2 sheet. Phys E. 2018;97:31.

[10] Mortazavi-Derazkola S, Salavati-Niasari M, Amiri O, Abbasi A. Fabrication and characterization of Fe_3O_4@ SiO_2@ TiO_2@ Ho nanostructures as a novel and highly efficient photocatalyst for degradation of organic pollution. J Energ Chem. 2017;26(1):17.

[11] Kavitha S, Jayamani N, Barathi D. Investigation on SnO_2/TiO_2 nanocomposites and their enhanced photocatalytic properties for the degradation of methylene blue under solar light irradiation. Bull Mater Sci. 2021;44(1):1.

[12] Ton NQT, Le TNT, Kim S, Dao VA, Yi J, Vu THT. High-efficiency photo-generated charges of ZnO/TiO_2 heterojunction thin films for photocatalytic and antibacterial performance. J Nanosci Nanotechnol. 2020;20(4):2214.

[13] Anku W, Oppong SOB, Shukla SK, Govender PP. Comparative photocatalytic degradation of monoazo and diazo dyes under simulated visible light using Fe^{3+}/C/S doped-TiO_2 nanoparticles. Acta Chim Slov. 2016;63(2): 380.

[14] Laishram D, Shejale KP, Gupta R, Sharma RK. Heterostructured HfO_2/TiO_2 spherical nanoparticles for visible photocatalytic water remediation. Mater Lett. 2018;231:225.

[15] Kaviyarasu K, Geetha N, Kanimozhi K, Magdalane CM, Sivaranjani S, Ayeshamariam A, Kenned J, Maaza M. In vitro cytotoxicity effect and antibacterial performance of human lung epithelial cells A549 activity of zinc oxide doped TiO_2 nanocrystals: investigation of bio-medical application by chemical method. Mater Sci Eng C. 2017;74:325.

[16] Zheng CH, Teng CP, Yang DP, Lin M, Win KY, Li ZB, Ye EY. Fabrication of luminescent TiO_2:Eu^{3+} and ZrO_2:Tb^{3+} encapsulated PLGA microparticles for bioimaging application with enhanced biocompatibility. Mater Sci Eng C. 2018;92:1117.

[17] Chen Y, Li S, Zhao RY, Li W, Ren ZH, Han GR. Single-crystal $TiO_2/SrTiO_3$ core-shell heterostructured nanowire arrays for enhanced photoelectrochemical performance. Rare Met. 2019; 38(5):369.

[18] Shi ZZ, Gao XX, Zhang HJ, Liu XF, Li HY, Zhou C, Yin YX, Wang LN. Design biodegradable Zn alloys: second phases and their significant influences on alloy properties. Bioact Mater. 2020;5(2):210.

[19] Han DL, Li Y, Liu XM, Yeung KWK, Zheng YF, Cui ZD, Liang YQ, Li ZY, Zhou SL, Wang XB, Wu SL. Photothermy-strengthened photocatalytic activity of polydopamine-modified metal-organic frameworks for rapid therapy of bacteria-infected wounds. J Mater Sci Technol. 2021;62:83.

[20] Kong XY, Liu XM, Zheng YF, Chu PK, Zhang Y, Wu SL. Graphitic carbon nitride-based materials for photocatalytic antibacterial application. Mater Sci Eng. 2021;145:100610.

[21] Zhu M, Liu XM, Tan L, Cui ZD, Liang YQ, Li ZY, Yeung KWK, Wu SL. Photo-responsive chitosan/Ag/MoS_2 for rapid bacteria-killing. J Hazard Mater. 2020;383:121122.

[22] Teng XF, Liu XM, Cui ZD, Zheng YF, Chen DF, Li ZY, Liang YQ, Zhou SL, Wu SL. Rapid and highly effective bacteria-killing by polydopamine/IR780@ MnO_2-Ti using near-infrared light. Prog Nat Sci: Mater Int. 2020;30(5):677.

[23] Han DL, Han YJ, Li J, Liu XM, Yeung KWK, Zheng YF, Cui ZD, Yang XJ, Liang YQ, Li ZY, Zhou SL, Yuan XB, Feng XB, Yang C, Wu SL. Enhanced photocatalytic activity and photothermal effects of Cu-doped metal-organic frameworks for rapid treatment of bacteria-infected wounds. Appl Catal B-Environ. 2020;261:118248.

[24] Xu YD, Liu XM, Zheng YF, Li CY, Yeung KWK, Cui ZD, Liang YQ, Zhu SL, Wu SL. Ag_3PO_4 decorated black urchin-like defective TiO_2 for rapid and long-term bacteria-killing under visible light. Bioact Mater. 2021;6(6):1575.

[25] Su K, Tan L, Liu XM, Cui ZD, Zheng YF, Li B, Han Y, Li ZY, Zhu SL, Liang YQ, Feng XB, Wang XB, Wu SL. Rapid photo-sonotherapy for clinical treatment of bacterial infected bone implants by creating oxygen deficiency using sulfur doping. ACS Nano. 2020;14(2):2077.

[26] Xue H, Chen YL, Liu XP, Qian QR, Luo YJ, Cui ML, Chen YS, Yang DP, Chen QH. Visible light-assisted efficient degradation of dye pollutants with biomass-supported TiO_2 hybrids. Mater Sci Eng C. 2018;82:197.

[27] Liang Y, Wang H, Casalongue HS, Chen Z, Dai HJ. TiO_2 nanocrystals grown on graphene as advanced photocatalytic hybrid materials. Nano Res. 2010;3(10):701.

[28] Chang SC, Zhang Q, Lu YK, Wu SZ, Wang W. High-efficiency and selective adsorption of organic pollutants by magnetic $CoFe_2O_4$/graphene oxide adsorbents: experimental and molecular dynamics simulation study. Sep Purif Technol. 2020;238: 116400.

[29] Liu JC, Bai HW, Wang YJ, Liu ZY, Zhang XW, Sun DD. Self-assembling TiO_2 nanorods on large graphene oxide sheets at a two-phase interface and their anti-recombination in photocatalytic applications. Adv Funct Mater. 2010;20(23):4175.

[30] Wang WJ, Li YC, Kang ZW, Wang F, Yu JC. A NIR-driven photocatalyst based on α-$NaYF_4$: Yb, Tm@ TiO_2 core–shell structure supported on reduced graphene oxide. Appl catal B-Environ. 2016;182:184.

[31] Mi C, Tian ZH, Cao C, Wang ZJ, Mao CB, Xu SK. Novel microwave-assisted solvothermal synthesis of $NaYF_4$: Yb, Er upconversion nanoparticles and their application in cancer cell imaging. Langmuir. 2011;27(23):14632.

[32] Kumar A, Reddy KL, Kumar S, Kumar A, Sharma V, Krishnan V. Rational design and development of lanthanide-doped $NaYF_4$@ CdS–Au–RGO as quaternary plasmonic photocatalysts for harnessing visible–near-infrared broadband spectrum. ACS Appl Mater Interfaces. 2018;10(18):15565.

[33] Rong XS, Qiu FS, Zhang C, Fu L, Wang YY, Yang DY. Preparation, characterization and photocatalytic application of TiO_2-graphene photocatalyst under visible light irradiation. Ceram Int. 2015;41(2):2502.

[34] Li D, Xu H. Rapid preparation of porous graphene microspheres supported TiO_2 for dye waste decoloration. Acta Microsc. 2020; 29(1):55.

[35] Ding J, Li BJ, Liu YS, Yan XS, Zeng S, Zhang XD, Hou LF, Cai Q, Zhang JM. Fabrication of Fe_3O_4@ reduced graphene oxide composite via novel colloid electrostatic self-assembly process for removal of contaminants from water. J Mater Chem A. 2015; 3(2):832.

[36] Zhang Y, Yuan SS, Zhao YH, Wang HG, He CD. Synthesis of novel yttrium-doped graphene oxide nanocomposite for dye removal. J Mater Chem A. 2014;2(21):7897.

[37] Zhang JJ, Qi P, Li J, Zheng XC, Liu P, Guan XX, Zheng GP. Three-dimensional Fe_2O_3–TiO_2–graphene aerogel nanocomposites with enhanced adsorption and visible light-driven photocatalytic performance in the removal of RhB dyes. J Ind Eng Chem. 2018;61:407.

[38] Kumar S, Sharma V, Bhattacharyya K, Krishnan V. Synergetic effect of MoS_2–RGO doping to enhance the photocatalytic performance of ZnO nanoparticles. New J Chem. 2016;40(6):5185.

[39] Zhang Y, Tang ZR, Fu XZ, Xu YJ. TiO_2-graphene nanocomposites for gas-phase photocatalytic degradation of volatile aromatic pollutant: is TiO_2-graphene truly different from other TiO_2−carbon composite materials? ACS Nano. 2010;4(12):7303.

[40] Zhang N, Zhang YH, Pan XY, Yang MQ, Xu YJ. Constructing ternary CdS–graphene–TiO_2 hybrids on the flatland of graphene oxide with enhanced visible-light photoactivity for selective transformation. J Phys Chem C. 2012;116(34):18023.

[41] Wang WJ, Zhang LZ, An TC, Li GY, Yip HY, Wong PK. Comparative study of visible-light-driven photocatalytic mechanisms of dye decolorization and bacterial disinfection by B-Ni-codoped TiO_2 microspheres: the role of different reactive species. Appl Catal B-Environ. 2011;108:108.

[42] Li Q, Guo BD, Yu JG, Ran JR, Zhang BH, Yan HJ, Gong JR. Highly efficient visible-light-driven photocatalytic hydrogen production of CdS-cluster-decorated graphene nanosheets. J Am Chem Soc. 2011;133(28):10878.

[43] An XQ, Jimmy CY, Wang F, Li CH, Li YC. One-pot synthesis of In_2S_3 nanosheets /graphene composites with enhanced visible-light photocatalytic activity. Appl Catal B-Environ. 2013; 129:80.

[44] Wang WJ, Chen XQ, Liu G, Shen ZR, Xia DH, Wong PK, Jimmy CY. Monoclinic dibismuth tetraoxide: a new visible-light-driven photocatalyst for environmental remediation. Appl Catal B-Environ. 2015;176:444.

[45] Hassani A, Çelikdag G, Eghbali P, Sevim M, Karaca S, Metin O. Heterogeneous sono-Fenton-like process using magnetic cobalt ferrite-reduced graphene oxide ($CoFe_2O_4$-rGO) nanocomposite for the removal of organic dyes from aqueous solution. Ultrason Sonochem. 2018;40:841.

[46] Yang CL, Liu J, Ren QH, Liu Y, Zhou P, Li H. Development of novel thermal sprayed hydroxyapatite-rare earth (HA-Re) coatings for potential antimicrobial applications in orthopedics. J Therm Spray Technol. 2021;30:886.

[47] Liu P, Liu Y, Lu ZX, Zhu JC, Dong JX, Pang DW, Shen P, Qu SS. Study on biological effect of La^{3+} on *Escherichia coli* by atomic force microscopy. J Inorg Biochem. 2004;98(1):68.

[48] Yang WD, Wang T, Lei HY, Liu JS. Progress in studies on biological effect of rare earth. Chin Rare Earth. 2000;21(3):62.